Hindawi
International Journal of Aerospace Engineering
Volume 2019, Article ID 2125976, 15 pages
https://doi.org/10.1155/2019/2125976

Research Article

Axial Spacing Effects on Rotor-Rotor Interaction Noise and Vibration in a Contra-Rotating Fan

Hengxuan Luan[1], **Liyuan Weng**[2], **Ranhui Liu**[1], **Dongmin Li**[1,3] and **Mingwei Wang**[4]

[1]*Department of Mechanical & Electronic Engineering, Shandong University of Science and Technology, Taian, China*
[2]*College of Geomatics, Shandong University of Science and Technology, Qingdao, China*
[3]*State Key Laboratory of Fluid Power and Mechatronic System, Zhejiang University, Hangzhou, China*
[4]*Shandong Taikai Electric Automation Co., Ltd, Taian, China*

Correspondence should be addressed to Hengxuan Luan; hengxuanluan@163.com

Received 20 March 2018; Revised 3 August 2018; Accepted 17 October 2018; Published 7 February 2019

Academic Editor: Seid H. Pourtakdoust

Because of the potential technical advantages, the contra-rotation technology has become a renewed interest in aviation and other applications. Contra-rotation increases efficiency in comparison with the single-rotor design, but this advantage is not fully harnessed. The axial spacing of two-stage contra-rotating blade rows has a significant impact on a contra-rotating fan/compressor. The results show that with a contra-rotation pattern, the strong unsteadiness of two-stage rotors is caused by the rotor-rotor interaction. The unsteadiness of rotor 1 is caused by the potential disturbance, and the upstream wake leads to the strong unsteadiness of rotor 2. With the increase of axial spacing, the rotor-rotor interaction is weakened, while unsteady features of two-stage rotor blades tend to be consistent. The acoustic and vibration effects of axial spacing are studied. It is found that the axial spacing has great influence of aerodynamic noise. The mean value of sound pressure level decreases by 17.2 dB in total when the axial spacing increased to 1.1 chord from 0.3 chord. For the accuracy of calculation, the scattering effect of the casing wall should be considered in the prediction of the noise. The axial spacing does not have obvious effects on the natural frequencies of the two-stage rotor blades but has certain effect on blade deformation.

1. Introduction

Turbomachinery is a joint name of power machinery capable of conversion between fluid energy and shaft power, wherein a continuously flowing fluid is taken as the working medium, and a continuous rotating blade is taken as the body. The design of modern turbomachinery has reached a very high level. The future development direction of the fan is higher performance, better reliability, more environmental protection, and lower noise level. The contra-rotation technology is one possible means for a more energy efficient turbomachinery. The contra-rotation technology offers significant improvements in the aerodynamic performance and the efficiency of axial flow fans, compressors, and turbines. Moreover, it also enables significant simplification in the machine structure and reduction in the machine size and weight.

Compared to ordinary two-stage axial flow fan, contra-rotating fan only consists of rotors, without stators. The rotating direction of two rotors is opposite. The second-stage impeller not only has the guide function same as the stator of ordinary axial flow fan but also adds energy to the air flow. As the stators are eliminated, the turbomachinery size is shortened, structure weight is reduced, and thrust-weight ratio can be greatly improved. In the aerodynamic aspect, on condition that aerodynamic layout is great, the aerodynamic loss will be able to be saved obviously and efficiency can be improved as well. The contra-rotating fan is a special design among the turbomachinery, whose flow field structure of the unique contra-rotating rotor is more research-oriented. The contra-rotating propeller was observed to give an improved flow through the slip-stream and leads to more efficient conversion of engine power to thrust. Lynam and Hawes [1] investigated a contra-rotating

fan and observed that it could provide a much higher pressure rise and through-flow capability at a higher efficiency. Through detailed experimental measurement, Roy et al. [2] changed rotation speed ratio and axial spacing of two-stage rotors, respectively, to research performance and characteristics of contra-rotating axial flow fans. Research results show that a large efficient running area could be obtained through the optimization of rotation speed matching and axial spacing of the front rotor and rear rotor. Pundhir [3] conducted the experimental research of a contra-rotating compressor and investigated the impacts of different casing shapes, rotation speed ratios, and axial spacing. Research results of MIT indicate that contra-rotating rotors can effectively increase aerodynamic loads of a fan/compressor. However, due to large airflow prerotation, the design of rotor 2 became more difficult [4]. Supported by the EU, the VITAL project aiming at research and development of novel aero-engines was initiated. The French SNECMA company developed a low-speed contra-rotating fan [5] and conducted experimental and numerical researches of the fan so as to compare characteristics of experimental, steady, and nonsteady flow fields [6]. Obviously, the contra-rotation technology is a development trend of turbomachines in the future. Most of above researches focus on the design or steady characteristics of contra-rotating fans/compressors. Flowing inside turbomachines is essentially periodical and unsteady, so more and more researches have started paying attention to unsteady phenomena in contra-rotating fans/compressors in recent years [7, 8]. Knapke and Turner [9] used an unsteady method to conduct numerical simulation of a contra-rotating compressor and concluded the details of the aspiration flow path choking mechanism. Gao et al. [10] pointed out that the unsteady property of a contra-rotating compressor is more special and the vibration and noise energy generated are stronger due to reverse rotation of the blade.

Blade faults seriously affect economic and safe running of turbomachinery. Most faults are caused by the blade fatigue which is mainly attributed to large dynamic stress of the blade and insufficient design of dynamic intensity. Therein, the dynamic stress intensity of the blade is mainly affected by blade vibration characteristics and unsteady airflow exciting force [11, 12]. Hoffmann et al. [13] applied the finite element method to compute self-vibration frequencies and vibration modes of blades, wherein computation programs included DLR's rotor simulation code S4 and ANSYS. Then, experimental methods were used to measure self-vibration frequency of the blade at different orders under nonrotation and rotation states, wherein the effectiveness of numerical modeling was verified. Palazotto and Shipman [14] assumed a two-dimensional turbine blade as a slab model, computed dynamic stress distribution and vibration amplitude of the turbine blade, and explored high-cycle fatigue courses of the blade. Xu et al. [15] researched stress and vibration of blades of a large axial flow fan by experiments and numerical simulation, finding that unsteady pressure fluctuation had very large effects on fan vibration characteristics. Poursaeidi et al. [16, 17] used ANSYS to research blade failure characteristics of a first-stage rotor of a gas compressor, finding that resonance under first-order and second-order natural frequencies was the major reason for blade fatigue cracking.

Figure 1: The view of contra-rotating axial fan.

A general expression for the sound field of a point force in arbitrary motion was found by Lowson [18] in 1965, followed by the expressions for the sound fields of a point acoustic stress in arbitrary motion. In recent years, in order to further reduce fan noise, the research focuses on three-dimensional sound source models, more sophisticated acoustic propagation models, and far-field acoustic radiation models [19]. Based on the FW-H equation, Maaloum et al. [20] analyzed aerodynamic acoustic performance computation established on the basis of an unsteady pressure field on the blade surface. Through theoretical analysis and experiments, Moreau and Oertwig [21] researched a single-stage high-speed fan and pointed out that the interference effect of wakes and outlet guide blade is the major reason for the generation of single-tone noise. Research results of Yang et al. [22] indicated that engines with application of the contra-rotation technology have low noise. However, research results of Wang et al. [23] indicate that contra-rotating fans can bring a serious noise problem.

As an important parameter of structural design of contra-rotating fan, the axial spacing between rotors has important impacts on various aspects. The dimension of axial spacing will directly influence the overall performance, noise, and vibration of contra-rotating fan. A large axial spacing can help weaken the unsteady interference effect between two stages, which will improve the aerodynamic noise performance and rotor safety. However, the aerodynamic performance can be affected once the axial spacing is too large. In the present study, for a contra-rotating fan, the unsteady behavior of flow, strength vibration characteristics, and noise level prediction are simulated using URANS, flow-solid coupling, and boundary element method. This paper makes preliminary summarization on the engineering applicability of contra-rotating fans in axial spacing.

2. Investigated Rig and Numerical Method

2.1. Description of Investigated Rig. The current investigation was performed on a contra-rotating axial flow fan. Figure 1 shows the picture of the contra-rotating fan (model: FBCDZ-no. 20). Used for aerodynamic design, rotor blades of front and rear rows are opposite in the direction of

Table 1: Design parameters of the contra-rotating axial fan.

Design parameter	Design speed (rpm)	Chord (tip/mid/hub) (mm)	Tip clearance (mm)
Rotor 1	−980	195.1/210.1/223.5	5
Rotor 2	980	194.8/209.7/222.6	5

rotation. Stator blades are not applied to aerodynamic design. The number of blades for the front rotor (rotor 1) and the rear rotor (rotor 2) was 19 and 17, respectively. The design volume flow of the fan was 64 m^3/s and the outer diameter was 2000 mm. The other main design parameters of the contra-rotating fan are shown in Table 1. In general, axial spacing refers to the axial distance between annular edges of two adjacent blades at the average radius position. For the present study, five fan configurations were investigated, with five sets of axial spacing dimensions being considered. The five axial spacing dimensions of the five investigated configurations were 0.3 chord, 0.5 chord, 0.7 chord, 0.9 chord, and 1.1 chord. The design axial spacing was 0.3 chord, while chord represents hub chord lengths of rotor 1.

2.2. Unsteady Flow Calculation. The governing equations are the unsteady compressible Navier-Stokes equations that describe the conservation of mass, momentum, and energy. In the conservative form, it can be expressed in three-dimensional coordinates as

$$\frac{\partial W}{\partial t} + \mathrm{div}F = 0, \tag{1}$$

where W is the vector of conservative variables, $F = (f - f_v, g - g_v, h - h_v)$ is the flux tensor; f, g, and h are the inviscid fluxes and f_v, g_v, and h_v are the viscous fluxes. The classical eddy viscosity assumption is made to compute turbulent fluxes necessary to close the system of URANS equations. The governing equations were solved with the CFX software that uses the finite volume method. Based on the backward Euler scheme, the time marching was performed by using an efficient implicit time integration scheme and was coupled with a second-order dual time stepping method. The turbulence model of Shear Stress Transport model was applied, referred to as SST model, which was combined with advantages of k-ω turbulence model in terms of simulating the near-wall boundary layer and characteristics of k-ε turbulence model concerning small dependence towards far-field boundary conditions.

No-slip and adiabatic conditions were applied to all wall surfaces; the total temperature and total pressure of standard atmosphere as well as axial inflow were specified as the inlet boundary condition, while the static pressure was specified at the outlet assuming radial equilibrium. The stage method was used to process the interface. With regard to flow field analysis, single-passage simulations were conducted.

The computational grid was generated by AUTOGRID5 software. A structured grid was used, and the computing grids were divided into domains of rotor 1 and rotor 2. The minimum grid spacing on the solid wall was 2×10^{-6} m

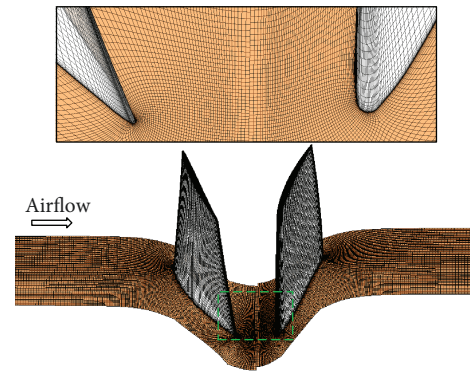

Figure 2: Mesh structure of contra-rotating fan.

that gives $y^+ < 2$ at the walls. Through grid independence verification, 2.9×10^6 grid nodes were applied for the computation in present work under consideration of computational accuracy and time.

With the increase of axial spacing, O4H topology structure was used as mesh in the area where two-stage rotors were located so as to ensure orthogonality and smoothness of meshes. Meanwhile, in order to fully apply the axial distance between two-stage rotors, the middle position between two adjacent rows of blades is often selected as the rotor-rotor interface, as shown in Figure 2. In addition, the butterfly topology was adopted to model the tip clearance of rotors. The numbers of stream-wise, span-wise, and pitch-wise grid nodes of both rotor 1 and rotor 2 are $123 \times 85 \times 91$.

2.3. Acoustic Source Computation. At first, the paper obtained numerical solutions of unsteady turbulent flow fields of the contra-rotating fan by URANS and extracted sound pressure pulsation signals on the blade surface as the sound source. Then, the acoustic wave equation was solved in the frequency domain and the radiation noise from the sound source to a far field was computed. In the paper, impacts of the average flow field on acoustic ration were neglected during acoustic field solution. The basic equation is a classical Helmholtz equation:

$$\nabla^2 p(x, y, z) + k^2 p(x, y, z) = 0, \tag{2}$$

where $k = \omega/c = 2\pi f/c$, k denotes the number of sound waves, ω denotes an angular frequency, c denotes a sound speed, and f denotes the frequency. With regard to external radiation, sound waves are propagated in unbounded space. Acoustic space V is the space enclosed by the sound source surface Ω_a and the infinite acoustic boundary Ω_∞. On the infinite acoustic boundary, sound waves satisfy nonreflection conditions.

In the formation and transmission of rotor-rotor interaction noise, if effects of the casing are taken into account, the sound wave transmission will be classified into transmission in the finite space. Sound waves will be influenced by the casing. In the formation and transmission of rotor-rotor interference noise, if effects of the casing are taken into account, the sound wave transmission will be classified into

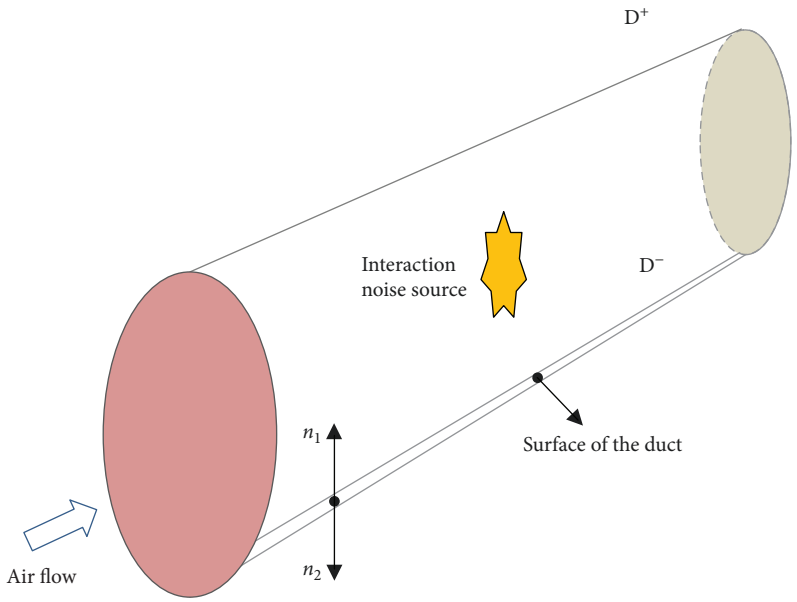

Figure 3: Schematic diagram of the BEM.

transmission in the finite space. Sound waves will be influenced by the casing. In acoustic calculation, acoustic analog method was applied to emission sound pressures. Boundary element method was applied to impacts of boundaries on acoustic wave transmission. The Helmholtz integral equation was solved. The acoustic model in the paper considered impacts of a fan duct, while acoustic boundary element meshes of the fan duct were introduced to acoustic boundary element computation. The schematic diagram of the BEM is shown in Figure 3. The sound field calculation domain is divided into an external domain D^+ and an internal domain D^-, and n_1 and n_2 represent normal unit vectors on both sides of the wall.

According to boundary element theories and in combination with Green formula and second Green formula, equation (2) can be converted into an integral equation based on the acoustic boundary, wherein G denotes a Green function which can be defined as follows, $C(r)$ is the positional parameter of the observation point:

$$\begin{cases} C(r)p(r) = \displaystyle\int_{\Omega_a} \left(p\frac{\partial G}{\partial n} + j\rho_0 \omega G v_n d\Omega_a \right), \\ G = \dfrac{e^{-jk|r-r_a|}}{4\pi|r-r_a|}, \end{cases} \tag{3}$$

where ρ_0 denotes the density of homogeneous medium in the sound field. As for observation point A in the acoustic space, when point A is located on the surface of duct, $C(r) = 1/2$ is satisfied, when point A is located in the external domain D^+, $C(r) = 1$ is satisfied. When point A is located in the internal domain D^-, $C(r) = 0$.

When the frequency is larger than 15,000 Hz, the sound pressure level will be very low. Hence, 15,000 Hz was selected as the maximum frequency $f_{\max}$ in the paper.

Figure 4: Schematic diagram of three-dimensional contra-rotating fan blades.

The transmission speed of sound in air is $c = 340$ m/s. According to equation (3), the maximum unit length $L_{\max}$ can be solved, $L_{\max} = 3.78$ mm. In the paper, the maximum mesh scale appeared in the radial direction. The maximum radial mesh scale was 0.03 mm, smaller than $L_{\max}$. Hence, acoustic computation requirements can be satisfied.

$$L_{\max} = \frac{c}{6f_{\max}}. \tag{4}$$

2.4. Fluid-Structure Calculation. Through the finite volume approach, iterative solution and discretization of NS equations were achieved. Heat transmission in flowing was explained through the solution of the total energy equation.

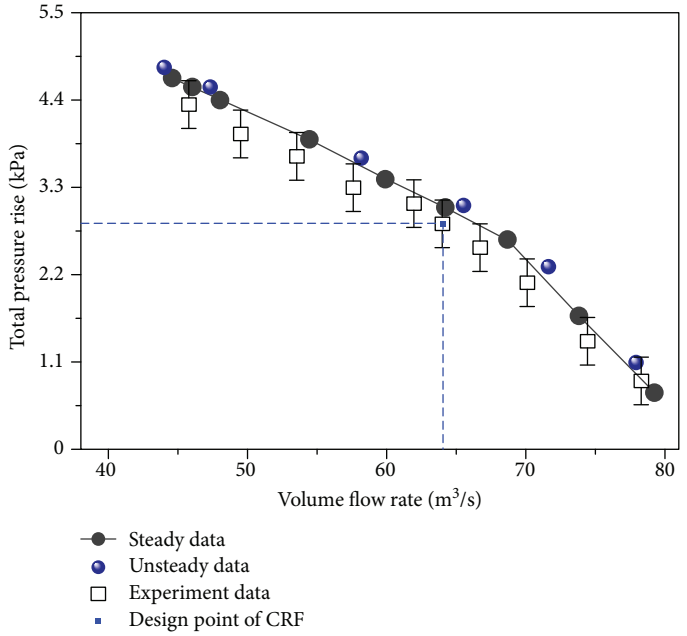

Figure 5: Curve of numerical and experimental performance of total pressure rise.

Fluid-solid couplings are explained through the solution of the dominant finite element matrix equations. Equation 5 and equation 6 involve elastic force and pressure force, respectively.

$$[M_s]\{\ddot{U}\} + [K_s]\{U\} = \{F_s\} + [R]\{P\}, \quad (5)$$

$$[M_f]\{\ddot{P}\} + [K_f]\{P\} = \{F_f\} - \rho_0[R]^T\{\ddot{U}\}, \quad (6)$$

where $[M]$ is the mass matrix, $[K]$ is the stiffness matrix, and $[F]$ is the force matrix, pertaining to both solid and fluid. $[R]$ is the "coupling" matrix that represents the effective surface area for each node on the fluid-structure interface. Directions of normal vectors of all the structural elements and fluid elements on the interface are presented in the coupling matrix. The direction leaving the fluid mesh and facing the structure is defined as the position direction. Functions of unconfirmed freedom node degrees are fluid loads and structural loads applied on the interface.

Before finite element analysis, the paper establishes the following assumptions:

(1) Welding of hub structures is completely reliable. All the structural parts are thoroughly welded, so welding residual stress does not exist

(2) Manufacture or installation deformation does not exist in the hub structure. Modeling is conducted according to ideal structures in the drawing during analysis

(3) Parts on the impeller are welded into a whole. The whole impeller is deemed as a whole body with continuous and uniform materials, wherein the density, elasticity modulus, and Poisson's ratio are consistent, namely, 2770 kg/m^3, 7.1×10^{10} Pa, and 0.33

Figure 4 is a comparison diagram of the finite element model and the actual blade. During the modeling of the paper, the structure of actual blade is simplified rationally. Firstly, small chamfers and rounding on parts are not embodied by the model, and effects of welding leg height on the structure are not considered. Secondly, transition fitting is adopted as the fitting between blade wheel axial hole and shaft; common flat key jointing is adopted; the blade wheel is completely fixed on the shaft; axial hole and two work faces of the key groove can be constrained fully; effects of the blade wheel shaft are not considered.

As for finite element analysis, grid types involved tetrahedral, hexahedral, and prism-shaped grids. The finite element models of two-stage rotor blades of the contra-rotating fan were established and the total number of grid units is 70,608.

3. Results and Discussion

3.1. Validation of Simulation. In order to verify the accuracy of numerical results, Figure 5 shows the numerical and experimental total pressure rise performance curve at the design speed of 0.3 chord axial spacing. The experiment had been conducted on the contra-rotating fan of which the design axial spacing, the detailed experimental steps can be found in the literature [7]. The numerical results were obtained from a number of steady and unsteady simulations, and the stall point was considered as the last operating point before nonconvergence. The agreement of overall performance curves between the numerical results and experiments can be observed for most parts.

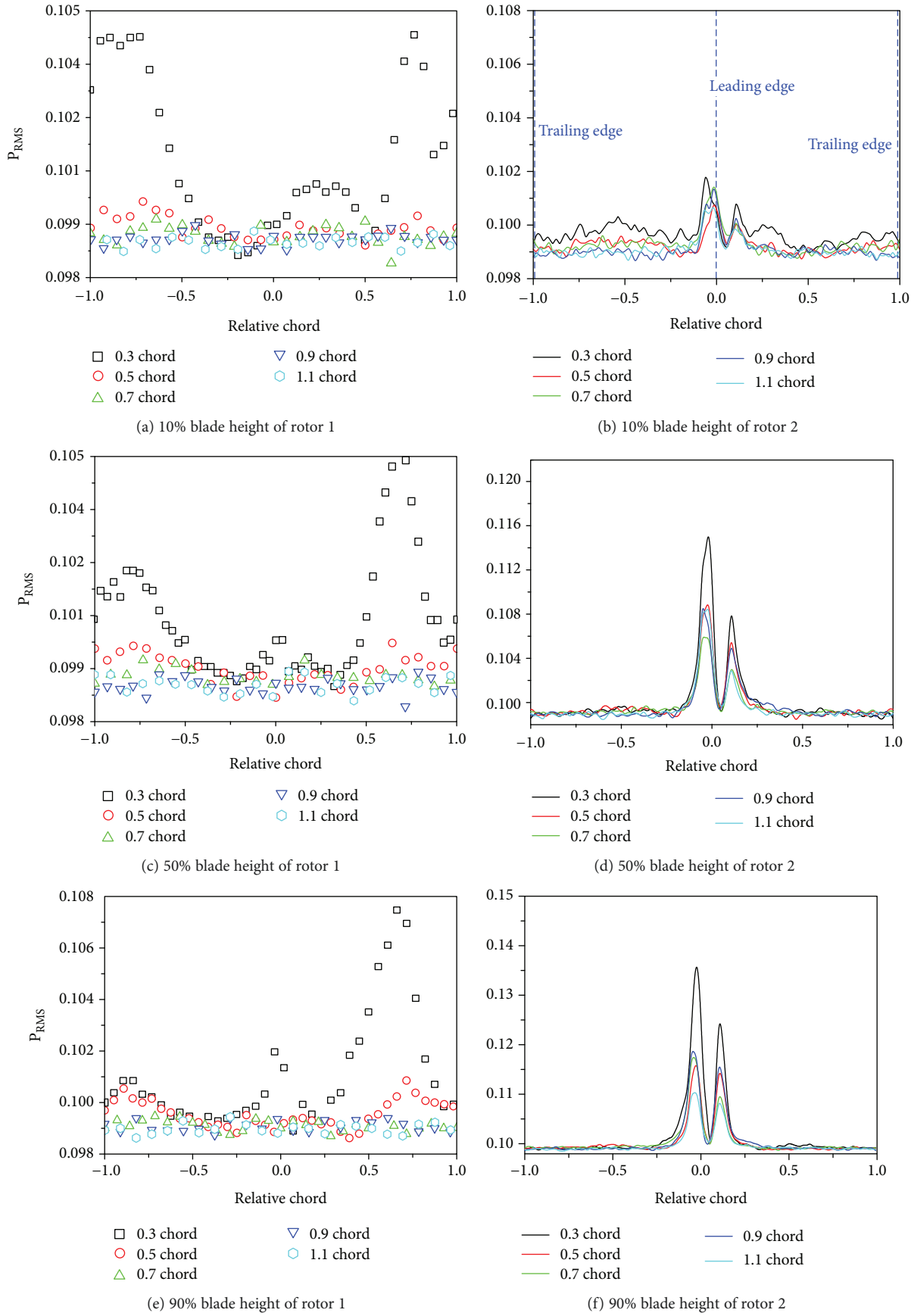

Figure 6: RMS pressure of two rotors at three typical spans with different axial spacing.

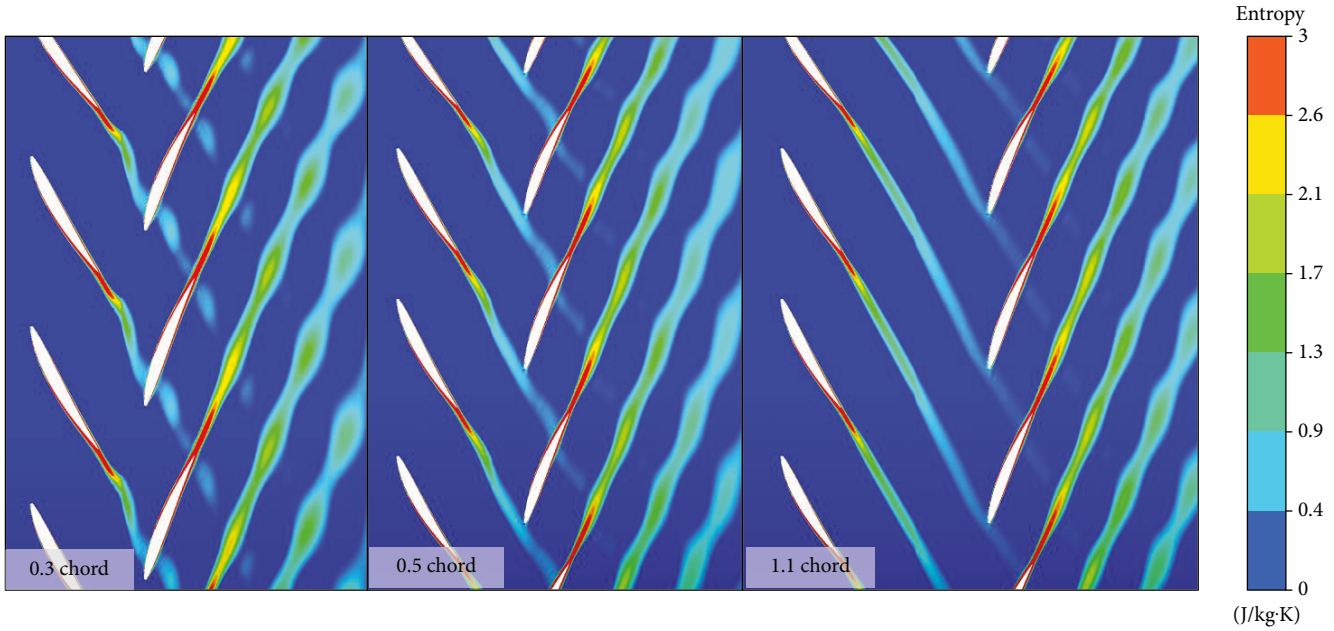

Figure 7: Contours of entropy at 50% blade height with respect to different axial spacing.

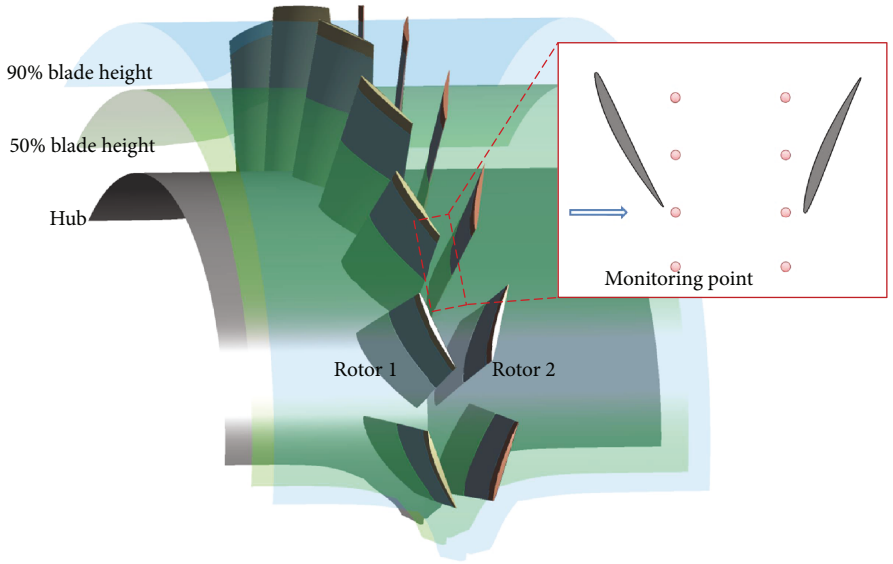

Figure 8: Diagram of numerical monitoring point distribution.

3.2. Unsteady Characteristic Analysis of Contra-Rotating Fan. Figure 6 shows RMS pressures of two-stage rotors with different axial spacing on three typical blade height cross sections, wherein the longitudinal coordinates denote RMS pressures, while horizontal coordinates denote relative chord lengths of blades. The RMS pressure formula is as follows:

$$P_{\mathrm{RMS}} = \left(\frac{\sqrt{(1/T)\int_0^T [p(z,r,\theta,t)]^2 dt}}{\bar{p}} - 0.99 \right) \times 1000, \quad (7)$$

where p denotes an unsteady value of pressure pulsation in flow fields; $\bar{p}$ denotes a time-average pressure of the flow field; T denotes an unsteady time cycle. RMS pressure denotes the unsteady pressure fluctuation strength acting on the blade surface.

On the overall level, as the axial spacing increased, significant decrease appeared to the unsteady fluctuation intensity of the static pressure on the surface of the blade. In addition, the maximum intensity of fluctuation suffered deflection. With regard to rotor 1, the obvious peaks of RMS pressure fluctuations existed in the root area of the blade when the

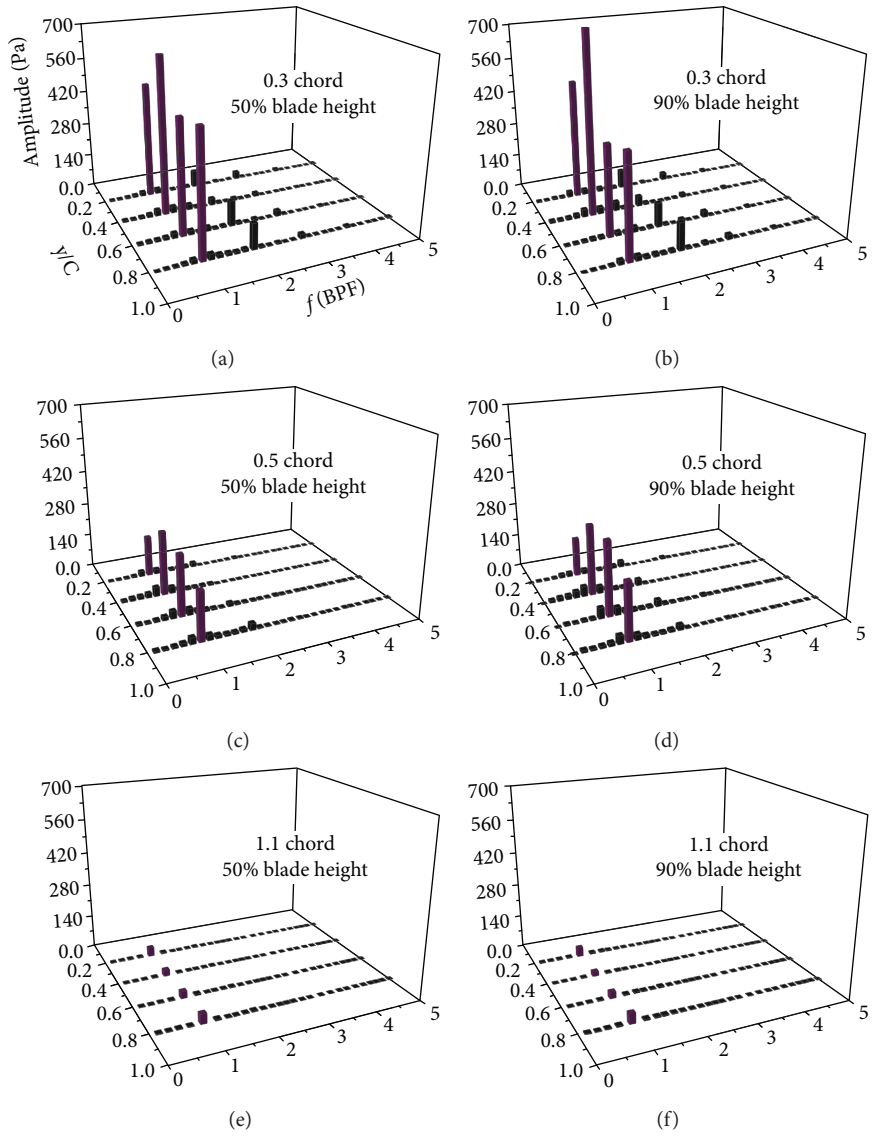

Figure 9: Frequency analysis of pressure fluctuation at trailing edge of rotor 1.

axial spacing was 0.3 chord. As the axial spacing was added to 0.5 chord, the degree of RMS pressure fluctuations decreased significantly, while the amplitudes of RMS pressure fluctuations turned quite weak after 0.9 chord. The contra-rotation of two-stage rotors will make the fluid expansion of upstream blade trailing edge restrained by the potential flow generated by the downstream rotor, directly resulting in more fierce pressure disturbance on the upstream rotor pressure surface than that of the suction surface. The phenomenon can be reflected to RMS pressure curve of rotor 1, as shown in the middle and top of impeller of rotor 1. The most obvious RMS pressure fluctuation appeared at axial spacing of 0.3 chord. Specifically, fluctuation peaks existed at the chord length 75% of that on the pressure surface, the blade leading edge as well as the place near the trailing edge on the suction surface. At the axial spacing of 0.5 chord, peaks of the RMS pressure fluctuation disappeared as for rotor 1; fluctuation peaks existed at the trailing edge on the suction surface and the chord length 70% of the relative chord length on the pressure surface; the amplitude had a significant decrease. The peaks of RMS pressure fluctuations disappeared after the axial spacing of 0.9 chord.

The rotor 2 at downstream was influenced by both the wake and potential flow interference of rotor 1 at upstream, while the contra-rotation made the relative speed of the inlet of rotor 2 increase sharply, and the air flow angle at its entrance will change drastically, which led to the acute static pressure fluctuations in the leading edge of rotor 2. With regard to rotor 2, on the curves of RMS pressure fluctuation showed two peaks at the height cross section of each blade and was located at the pressure surface and the suction surface of the leading edge on the blade. Specifically, the maximum amplitude of fluctuation existed at the axial spacing of 0.3 chord. As the axial spacing increased, the peak of the RMS pressure fluctuations decreased. The amplitude of RMS pressure fluctuations did not decrease obviously after the axial spacing of 0.5 chord.

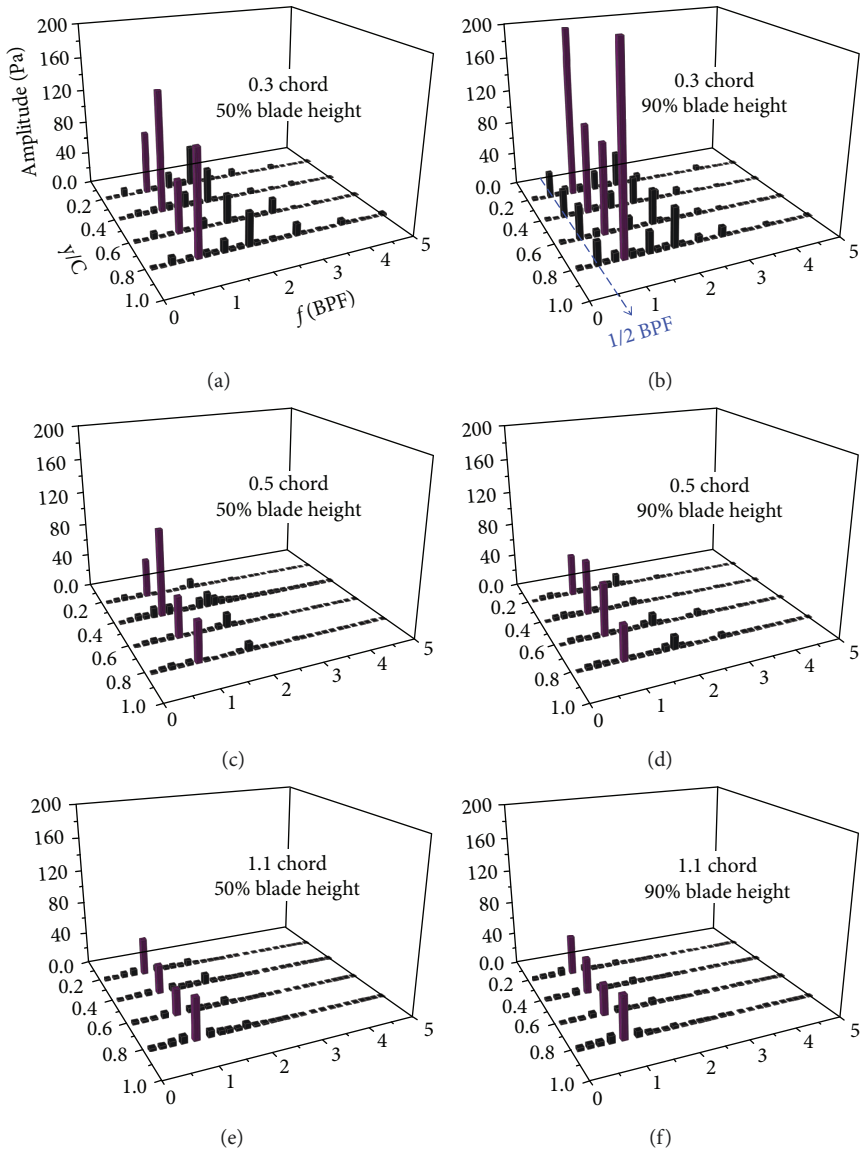

Figure 10: Frequency analysis of pressure fluctuation at leading edge of rotor 2.

In order to observe the rotor-rotor interaction between the two-stage rotors under different axial spacing more clearly, Figure 7 shows the entropy contour at the given time for unsteady calculation under different axial spacing, and the 50% relative blade height cross section is selected for the section. Wakes in the rotor-rotor interference effect occupy an important position. The wake had dual characteristics of velocity loss and vortex, quite different from the mainstream. Therefore, the existence of wake was one of the important factors that lead to the overall performance degradation of the fan. The figure can clearly display the movement patterns of wake from upstream. In the wake transport process, the mixing velocity was related to wake oscillation and the air flow viscous loss was also closely related to wake oscillation. It is found that in the 0.3 chord axial spacing, there is obvious wake oscillation, and the amplitude of wake oscillation decreases with the increase of the axial spacing, but the wake width is slightly increased. The increase of blade row spacing will lead to the interference intensity reduction between blades, which were the main reasons for the decrease of wake oscillation intensity with the increase of axial spacing. When the axial spacing was relatively large, the wake oscillation at upstream will disappear, indicating that the upstream wake oscillation is driven by the downstream rotor. The wake of rotor 1 was affected by the potential disturbance of rotor 2; the amplitude reduction of wake oscillation shows the weakening of the potential disturbance.

Fast Fourier Transform was conducted to static pressure fluctuation curves of a series of monitoring points in the flow field. 16 numerical monitoring points were arranged in a computation domain of a relative coordinate system of two-stage rotors in the paper, as shown in Figure 8. The monitoring points were located on the outlet side of rotor 1 and the inlet side of rotor 2. Four monitoring points were arranged on 50% blade height cross section and the 90%

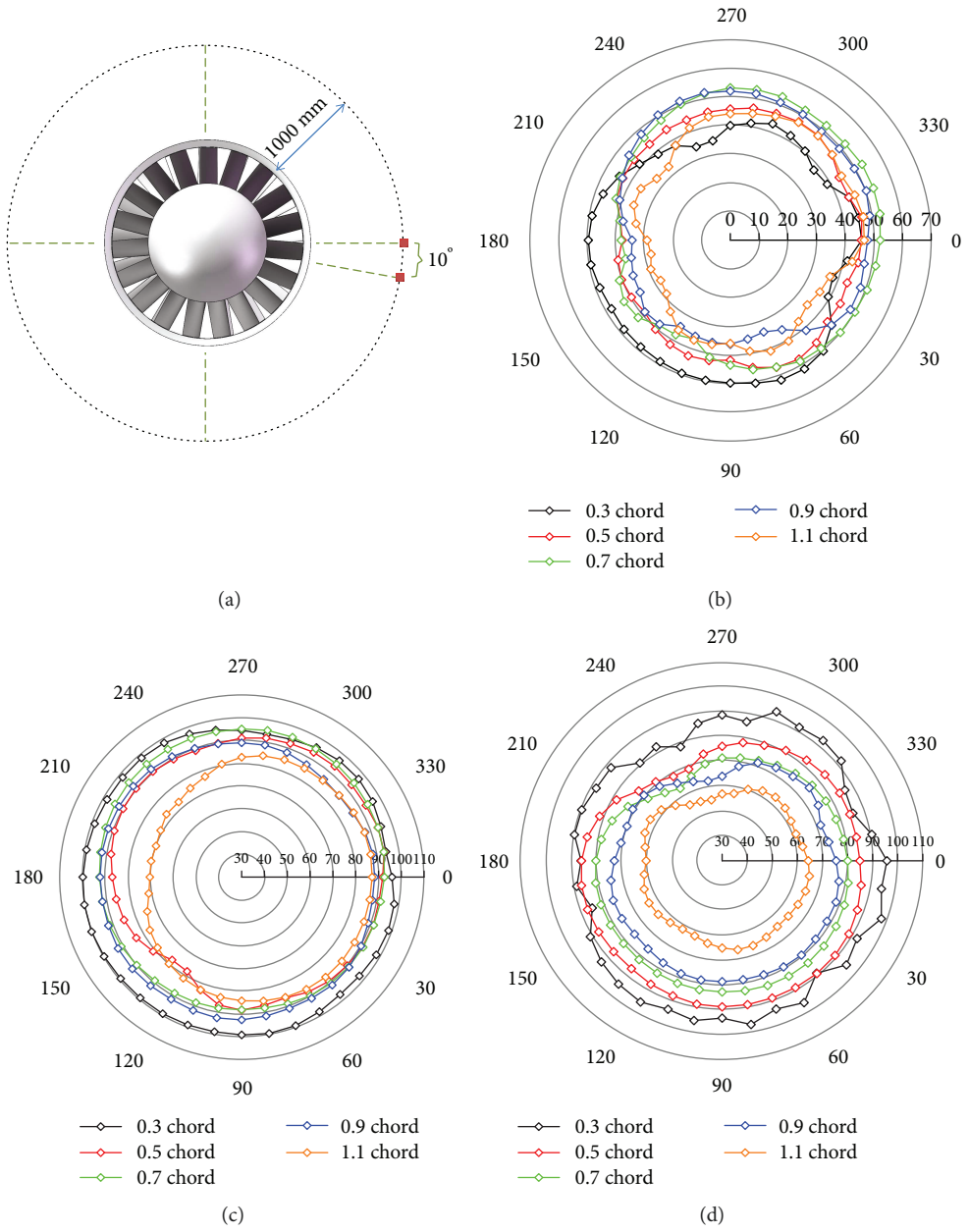

Figure 11: The monitoring point diagram and directivity curve of CRF under different axial spacing. (a) Monitoring point diagram. (b) 310 Hz. (c) 620 Hz. (d) 930 Hz.

blade height cross section of rotor 1 and were distributed averagely along the circumference. Monitoring points were arranged for rotor 2 with the same method.

Figures 9 and 10 display static pressure spectrograms at two typical blade height cross sections of rotor 1 and rotor 2 under different axial spacing. It is shown in the diagrams that main frequencies of static pressure fluctuations of rotor 1 and rotor 2 under different axial spacing were corresponding to blade passing frequency (BPF). Results indicate that flow field static pressure pulsation at the rotor 1 outlet was mainly affected by the potential disturbance of rotor 2; the flow field at the inlet of rotor 2 was affected by the upstream potential disturbance. In addition, under the axial spacing of 0.3 chord, 1/2 BPF could be monitored in static pressure fluctuation frequency constitution of rotor 2 at the 90% blade height cross section (Figure 9(b)), while this frequency was tip leakage vortex frequency. This shows that the blade tip area was obviously affected by tip leakage vortex under small axial spacing.

By comparing different conditions of axial spacing, we find that when the axial spacing is 0.3 chord, static pressure fluctuation amplitude of rotor 1 was far larger than that of rotor 2; flow field static pressure fluctuation frequencies at the outlet of rotor 1 were mainly the BPF and twice its frequency; more fractional frequencies appeared in the static pressure spectrogram of flow field at the inlet of rotor 2, including 1/2 BPF, 3/2 BPF, and 2 BPF. With the increase of axial spacing, static pressure fluctuation amplitudes of

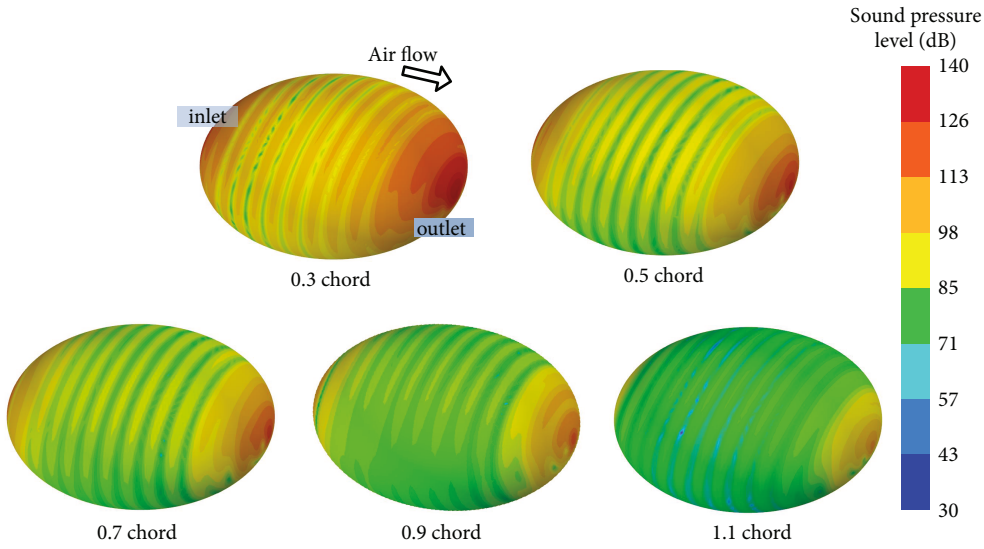

Figure 12: Schematic diagram of the acoustic calculation area.

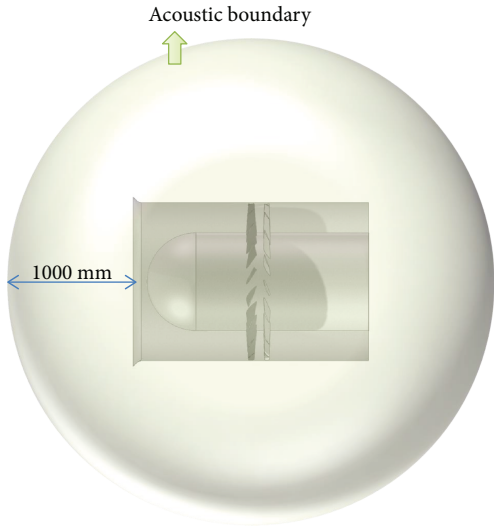

Figure 13: Contour of far-field radiation noises of the contra-rotating fan under different axial spacing.

two stages were basically equivalent under the axial spacing of 1.1 chord; amplitudes of fractional frequencies were very small; and distribution of static pressure fluctuation frequencies of two-stage monitoring points tended to be consistent. The result indicated that under the small axial spacing, interactions between two rotors were violent, as affected by upstream wakes and complicated eddies, and the inlet flow field of rotor 2 was more complicated. With the increase of axial spacing, interactions were weakened, and airflow flowing at the inlet of rotor 2 was more uniform.

3.3. Acoustic Far-Field of Contra-Rotating Fan. As for the CRF, interaction exists between two-stage rotors. Because of the effects of the potential flow field and wakes, airflows are nonuniform after passing the rotor blades. When the rotors are rotating, the blades will face the nonuniform incoming flow of which the incidence airflow angle keeps on changing, so that the lift force on the blade will change then. The reactive force of the fluid towards pulsation lift force of the blade, namely, the pulsation force of blades acting on the fluid, will lead to occurrence of a sound field. In addition, rotational noise of the rotor also includes discrete noise caused by cyclic changes of the airflow speed and broadband noise caused by turbulent flows.

In an actual axial flow fan, because of the existence of the casing wall boundaries, the transmission of sound waves will be influenced obviously. Moreover, the axial spacing will also bring significant influences to the interference noise. Noise spectrums and directions of spatial points located at different positions of sound field are different. Figure 11 shows the monitoring point diagram and directivity curve of contra-rotating fan. Figure 11(a) shows that the rotation center of rotor 1 was set as the center of circle; a round monitoring curve of which distance from fan casing was 1000 mm, and a monitoring point was set at the interval of 10° on the curve for analysis of radiation sound fields.

Figure 11 shows the diagrams of far-field noise directivity curves of the contra-rotating fan under different axial spacing. Where Figure 11(b)–11(d) denotes the noise curve under frequencies of 310 Hz, 620 Hz, and 930 Hz. The blade passing frequency (BPF) was 620 Hz. On the whole, under different axial spacing, the contra-rotating fan basically showed the same capacity of noise radiation in different directions. As the axial spacing increased, the mean value of sound pressure level of the monitoring curve of contra-rotating fan showed a decreased trend. Noise directivity curves under different frequencies were compared. The far-field noise was maximum at 620 Hz (BPF). The smaller the axial spacing is, the more significant the BPF noise would be in comparison with other frequencies. Hence, only noise characteristics of BPF will be analyzed.

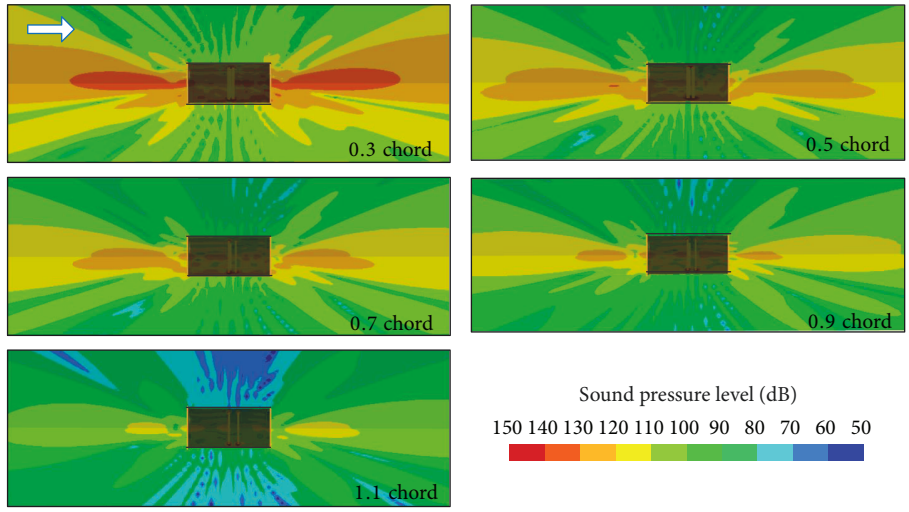

Figure 14: The acoustic field of contra-rotating fan under different axial spacing.

As shown in Figure 11(c), under different axial spacing, the mean value of sound pressure level decreased by 8.8 dB when the axial spacing increased to 0.5 chord from 0.3 chord. The mean value of sound pressure level increased by 1.5 dB when it increased to 0.9 chord from 0.5 chord. It indicated that at the axial spacing of 0.3–0.9 chord, the minimum interaction noise of the contra-rotating fan appeared at 0.5 chord. The reason is that the flow interaction between two-stage rotors was organized well at the axial spacing of 0.5 chord, and amplitudes and phases of pressure fluctuations on the blade surface were well controlled. The mean value of sound pressure level decreased by 8.4 dB when the axial spacing increased to 1.1 chord from 0.9 chord. The mean value of sound pressure level decreased by 17.2 dB in total when the axial spacing increased to 1.1 chord from 0.3 chord. This result indicates that with the further increase in axial spacing, the interaction effects of two-stage rotors were gradually weakened, and the interaction noise generated decreased obviously. However, in the aerodynamic design of contra-rotating fan, the axial spacing which is too large will lead to a decrease in aerodynamic performance.

In order to more easily observe the situation of the radiated sound field, Figure 12 is the schematic diagram of the calculation area of acoustic boundary element method. In the computational domain of acoustic boundary element method, air was the medium, with a density of 1.225 kg/m^3 and acoustic propagation speed of 340 m/s, while metal was defined as the fan duct material.

Figure 13 shows the contour of far-field radiation noise of the contra-rotating fan under different axial spacing. With regard to each spherical surface contour of the contra-rotating fan, the far-field noise distribution was symmetric to a certain extent. The noise is larger on the inlet and outlet sides of the fan, smaller in the casing side, as the noise radiation of the contra-rotating fan was affected by the fan duct. As for sound pressure levels of far-field radiation noise of the contra-rotating fan under different axial spacing, the maximum sound pressure level appeared under 0.3 chord and the minimum value appeared under 1.1 chord. The radiation noise was on the decline under the axial spacing ranging from 0.3 to 1.1, and it varied gently.

In order to know the distribution characteristics of sound fields under influences of wall boundaries of the casing more clearly, Figure 14 gives the sound field distribution cross section diagram of interaction noise of the contra-rotating fan. It is shown in the diagram, in the propagation to the far field, sound waves were mainly interfered by the wall boundaries. In the casing, the sound pressure level of the sound field was higher than that of the external sound field as sound waves were accumulated in the pipeline because of rigid sound impedance effects brought by boundaries to sound waves. Outside the casing, sound waves were gradually attenuated during propagation. In different propagation directions, sound field distribution was obviously different.

3.4. Vibration Strength Characteristics of Contra-Rotating Fan. Table 2 displays the computation results of two-stage rotor blades under the first 6 orders of natural frequencies based on schemes with different axial spacing. Results indicate that with the increase of axial spacing, natural frequencies of two-stage blades were basically unchanged. The reason is that the blade natural frequency was mainly affected by centrifugal inertia loading and was only slightly affected by aerodynamic force loading. Affecting degree of axial spacing on aerodynamic loading of two-stage rotor blades did not have obvious effects on blade vibration characteristics. Hence, natural frequencies of the two-stage blades were only affected slightly by changes of the axial spacing.

Figure 15 displays the histograms of maximum total deformation and maximum equivalent stress of two-stage rotor blades under different axial spacing. It represents maximums of total deformation and maximum equivalent stress (von Mises Stress on the blades). It is shown in the diagram, with the increase of axial spacing, the deformation and stress of two-stage rotor blades tended to decrease as a whole. With the changing of the axial spacing, the maximum

Table 2: The natural frequency of the first 6 steps of the blades with different axial spacing.

(a) Rotor 1

Order	Natural frequency of rotor 1/(Hz)				
	0.3 chord	0.5 chord	0.7 chord	0.9 chord	1.1 chord
1	182.41	182.42	182.42	182.41	182.39
2	584.51	584.52	584.53	584.5	584.46
3	725.69	725.71	725.78	725.73	725.6
4	1234	1234	1234	1234	1234
5	1328.6	1328.6	1328.7	1328.6	1328.5
6	1667.1	1667.2	1667.4	1667.2	1666.9

(b) Rotor 2

Order	Natural frequency of rotor 2/(Hz)				
	0.3 chord	0.5 chord	0.7 chord	0.9 chord	1.1 chord
1	179.5	179.49	179.47	179.51	179.49
2	577.03	577	576.96	576.98	577.04
3	724.62	724.56	724.43	724.63	724.63
4	1208.8	1208.8	1208.7	1208.8	1208.8
5	1318.7	1318.6	1318.5	1318.6	1318.7
6	1656.4	1656.3	1655.9	1656.3	1656.5

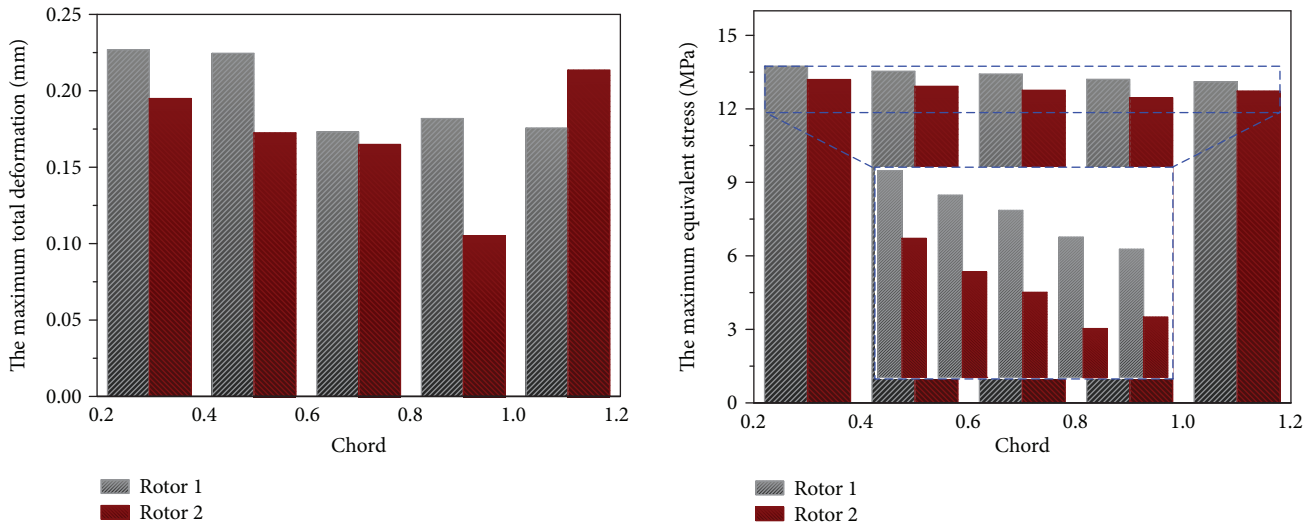

Figure 15: The max total deformation and equivalent stress of two blades of the contra-rotating fan.

total deformation of two-stage rotor blades embodied great differences in changing amplitude; the maximum equivalent stress of two-stage rotor blades had the consistent changes.

With the increase of axial spacing, the blade deformation of rotor 1 changed obviously after 0.5 chord and the blade deformation of rotor 2 decreased obviously after 0.7 chord. Moreover, the effects of axial spacing changes on the deformation of the rotor 2 blade were more obvious. As for the equivalent stress of blades, within the certain scope of axial spacing, the vibration stress of downstream rotor blades was mainly sourced from pressure fluctuations on the blade surface caused by upstream wakes. Research results of wakes mentioned above show that with the increase of axial spacing, the wake strength decreased gradually and the wake width increased gradually. Hence, the pressure fluctuation amplitude decreased along the flow direction. Meanwhile, the strength of downstream potential interference was gradually weakened. Hence, the equivalent stress of two-stage rotors tended to decrease with the increase of axial spacing.

4. Conclusion

(1) Under different axial spacing, main frequencies of static pressure fluctuations of rotor 1 and rotor 2 were corresponding to BPF (twice the blade passing frequency of each rotor). Under the axial spacing of 0.3 chord, the static pressure fluctuation amplitudes of two-stage rotors were maximum, while the fractional frequency amplitudes were large as well. With the increase of axial spacing, the rotor-rotor interactions were weakened, while unsteady features of two-stage rotor blades tended to be consistent, and static pressure fluctuation amplitudes of rotors decreased

(2) The mean value of sound pressure level decreased by 17.2 dB in total when the axial spacing increased to 1.1 chord from 0.3 chord. When axial spacing was less than 0.5 chord, the axial spacing had a large effect on the noise level. It is found that the axial spacing had little effect on radiation noise, when the axial spacing varies in the range of 0.5–0.9 chord

(3) Considering the scattering effect of the casing wall, the acoustic effect of interaction noise radiated was studied. The results showed that sound waves were interfered by the wall boundaries of casing; therefore, the effect of the casing wall should be considered in the acoustic calculation of an actual axial flow fan

(4) As a whole, axial spacing did not have obvious effects on natural frequencies of the two-stage rotor blades but had certain effect on blade deformation. In comparison with the rotor 1 blade, the maximum total deformation of the rotor 2 blade was affected by the axial spacing more obviously

Data Availability

The data of the article is temporarily unavailable and can be disclosed after the article is published.

Conflicts of Interest

The authors declare that they have no conflicts of interest.

Acknowledgments

The authors would like to acknowledge the support of National Key R&D Program of China (2018YFC0604702), the support of Scientific Research Foundation of Shandong University of Science and Technology for Recruited Talents (Grant no. 2017RCJJ078), the support of Key Research and Development Plan of Shandong Province (Grant no. 2017GSF220010), the support of Open Foundation of the State Key Laboratory of Fluid Power Transmission and Control (Grant no. GZKF-201614).

References

[1] F. C. Lynam and S. P. Hawes, "Contra rotating axial flow fans," *The Engineers*, pp. 1–8, 1946.

[2] B. Roy, K. Ravibabu, P. Srinivasa Rao, S. Basu, A. Raju, and P. N. Murthy, "Flow studies in ducted twin-rotor contra-rotating axial flow fans," in *ASME 1992 International Gas Turbine and Aeroengine Congress and Exposition*, p. 8, Cologne, Germany, 1992.

[3] D. S. Pundhir, "A study of some factors affecting the effectiveness of casing treatment in a contra-rotating axial compressor stage," *Indian Journal of Engineering & Materials Sciences*, vol. 1, no. 4, pp. 199–207, 1994.

[4] J. H. Freedman, *Design of a Multi-Spool, High-Speed, Counter-Rotating Aspirated Compressor*, Massachusetts Institute of Technology, 2000.

[5] J. Talbotec and M. Vernet, "Snecma counter rotating fan aerodynamic design logic & tests results," in *27th International Congress of Aeronautical Sciences*, pp. 19–24, Nice, France, 2010.

[6] T. Lengyel-Kampmann, A. Bischoff, R. Meyer, and E. Nicke, "Design of an economical counter rotating fan: comparison of the calculated and measured steady and unsteady results," in *ASME Turbo Expo 2012: Turbine technical conference and exposition*, pp. 323–336, Copenhagen, Denmark, 2012.

[7] H. X. Luan, L. Weng, and Y. Z. Luan, "Numerical simulation of unsteady aerodynamic interactions of contra-rotating axial fan," *PLoS One*, vol. 13, no. 7, article e0200510, 2018.

[8] H. X. Luan, L. Y. Weng, R. H. Liu, Y. Z. Luan, and D. M. Li, "Investigation of speed matching affecting contrarotating fan's performance using wireless sensor network including big data and numerical simulation," *Complexity*, vol. 2018, Article ID 1246381, 12 pages, 2018.

[9] R. D. Knapke and M. G. Turner, "Unsteady simulations of a counter-rotating aspirated compressor," in *ASME Turbo Expo 2013: Turbine Technical Conference and Exposition*, p. 13, San Antonio, TX, USA, 2013.

[10] L. M. Gao, F. Miao, R. Y. Li, and B. Liu, "Effect of rotor/rotor interactions on blades unsteady loading," *Acta Aeronautica et Astronautica Sinica*, vol. 35, no. 7, pp. 1874–1881, 2014.

[11] C. Lawson and P. Ivey, "Tubomachinery blade vibration amplitude measurement through tip timing with capacitance tip clearance probes," *Sensors and Actuators A: Physical*, vol. 118, no. 1, pp. 14–24, 2005.

[12] H. Diken and K. Alnefaie, "Effect of unbalanced rotor whirl on blade vibrations," *Journal of Sound and Vibration*, vol. 330, no. 14, pp. 3498–3506, 2011.

[13] F. Hoffmann, R. Keimer, and J. Riemenschneider, "Structural modeling and validation of an active twist model rotor blade," *CEAS Aeronautical Journal*, vol. 7, no. 1, pp. 43–55, 2016.

[14] A. Palazotto and W. Shipman, "The consideration of high cycle fatigue in a turbine blade," in *43rd AIAA/ASME/ASCE/AHS/ASC Structures, Structural Dynamics, and Materials Conference, Structures, Structural Dynamics, and Materials and Co-located Conferences*, Denver, CO, USA, 2006.

[15] C. Xu, R. S. Amano, and E. K. Lee, "Investigation of an axial fan—blade stress and vibration due to aerodynamic pressure field and centrifugal effects," *JSME International Journal*, vol. 47, no. 1, pp. 75–90, 2004.

[16] E. Poursaeidi, A. Babaei, M. R. Mohammadi Arhani, and M. Arablu, "Effects of natural frequencies on the failure of R1 compressor blades," *Engineering Failure Analysis*, vol. 25, no. 10, pp. 304–315, 2012.

[17] L. Jiang, Q. Wu, Q. Wu et al., "Fracture failure analysis of hard and thick key layer and its dynamic response characteristics," *Engineering Failure Analysis*, 2019.

[18] M. V. Lowson, "The sound field for singularities in motion," *Proceedings of the Royal Society A: Mathematical, Physical and Engineering Sciences*, vol. 286, no. 1407, pp. 559–572, 1965.

[19] N. Peake and A. B. Parry, "Modern challenges facing turbomachinery aeroacoustics," *Annual Review of Fluid Mechanics*, vol. 44, no. 1, pp. 227–248, 2012.

[20] A. Maaloum, S. Kouidri, and R. Rey, "Aeroacoustic performance evaluation of axial flow fans based on the unsteady pressure field on the blade surface," *Applied Acoustics*, vol. 65, no. 4, pp. 367–384, 2004.

[21] A. Moreau and S. Oertwig, "Measurements compared to analytical prediction of the sound emitted by a high-speed fan stage," in *19th AIAA/CEAS Aeroacoustics Conference, Aeroacoustics Conferences*, Berlin, Germany, 2013.

[22] L. Yang, L. Chen, H. Sun, and M. S. Yang, "Investigation of counter rotating fan design technology," *Acta Aeronautica et Astronautica Sinica*, vol. 35, no. 5, pp. 1226–1235, 2014.

[23] J. Wang, F. Ravelet, and F. Bakir, "Experimental comparison between a counter-rotating axial-flow fan and a conventional rotor-stator stage," in *10th European Turbomachinery Conference*, p. 1, Lappeenranta, Finland, 2013.